



# Magnetic phases of the frustrated ferromagnetic spin-trimer system $\text{Gd}_3\text{Ru}_4\text{Al}_{12}$ with a distorted kagome lattice structure

S. Nakamura <sup>1,2,\*</sup>, N. Kabeya <sup>2,3</sup>, M. Kobayashi,<sup>3</sup> K. Araki,<sup>4</sup> K. Katoh,<sup>4</sup> and A. Ochiai<sup>2,3</sup>

<sup>1</sup>*Institute for Materials Research, Tohoku University, Katahira, Sendai 980-8577, Japan*

<sup>2</sup>*Center for Low Temperature Science, Tohoku University, Katahira, Sendai 980-8577, Japan*

<sup>3</sup>*Department of Physics, Tohoku University, Aramaki, Sendai 980-8578, Japan*

<sup>4</sup>*Department of Applied Physics, National Defense Academy, Yokosuka 239-8686, Japan*



(Received 28 November 2018; revised 10 January 2023; accepted 12 January 2023; published 26 January 2023)

Magnetization and specific heat measurements were conducted on single-crystalline  $\text{Gd}_3\text{Ru}_4\text{Al}_{12}$ , in which magnetic Gd–Al layers with a distorted Kagome lattice structure and nonmagnetic Ru–Al layers are stacked alternately along the  $c$  axis. A previous study indicated that the distorted Kagome lattice structure of Gd–Al layers effectively translates into an antiferromagnetic (AFM) triangular lattice in association with ferromagnetic (FM) spin trimerization at low temperatures. The present results indicate that the spin system of  $\text{Gd}_3\text{Ru}_4\text{Al}_{12}$  has two types of anisotropies: easy-plane-type and easy-axis-type anisotropies. The trimers carry magnetic quadrupole moments when the FM directivity of the component spins is imperfect. The origin of the unusual magnetic anisotropies that were observed can be explained by the magnetic quadrupole interactions that take place between the trimers. The stability of a helical structure in the crystal with inversion-symmetry is discussed.

DOI: [10.1103/PhysRevB.107.014422](https://doi.org/10.1103/PhysRevB.107.014422)

## I. INTRODUCTION

Metallic  $4f$  frustrated spin systems often exhibit peculiar features at low temperatures. The ternary intermetallic compounds  $RE_3\text{Ru}_4\text{Al}_{12}$  ( $RE$ : rare earth) crystallize in a hexagonal structure of the  $\text{Gd}_3\text{Ru}_4\text{Al}_{12}$  type, which belongs to the space group  $P6_3/mmc$  (No. 194) [1]. In this crystal, magnetic  $RE$ -Al layers and nonmagnetic Ru-Al layers stack alternately along the  $c$  axis [Figs. 1(a) and 1(b)] [2]. As shown in Fig. 1(c), the  $RE$  ions form a distorted Kagome lattice or a breathing Kagome lattice composed of two different sized regular triangles and hexagons with unequal sides. The system  $RE_3\text{Ru}_4\text{Al}_{12}$  has been investigated extensively because of the various phenomena it exhibits at low temperatures. Specifically,  $\text{La}_3\text{Ru}_4\text{Al}_{12}$  is Pauli paramagnetic (PM) and  $\text{Pr}_3\text{Ru}_4\text{Al}_{12}$  and  $\text{Nd}_3\text{Ru}_4\text{Al}_{12}$  are FM [3–6], whereas  $\text{Ce}_3\text{Ru}_4\text{Al}_{12}$  is believed to be a valence fluctuation system [1]. When  $RE$  sites are replaced by heavy  $RE$  ions,  $RE_3\text{Ru}_4\text{Al}_{12}$  becomes AFM.  $\text{Yb}_3\text{Ru}_4\text{Al}_{12}$  is an  $XY$  antiferromagnet with Néel order at  $T_N = 1.5$  K [7,8]. This compound is a heavy fermion system with enhanced Sommerfeld coefficients  $\gamma_0 = 120$  mJ/(K<sup>2</sup> Yb-mol).  $\text{Dy}_3\text{Ru}_4\text{Al}_{12}$  is an AFM compound with  $T_N = 7$  K, which has a noncollinear spin structure [9]. Regardless of the long-range AFM ordering, this compound has a large  $\gamma_0$  value of approximately 500 mJ/(K<sup>2</sup> Dy-mol) in the temperature range 7–20 K. Gorbunov *et al.* attributed this large  $\gamma_0$  value to spin fluctuations, which are induced in the Ru  $4d$  electrons by the exchange field resulting from Dy  $4f$  electrons [9]. Chandragiri *et al.* reported spin glass characteristics similar to the dynamics in  $\text{Dy}_3\text{Ru}_4\text{Al}_{12}$  in the AFM phase,

which indicates a complex ground state under the influence of geometrical frustration [10].

In 2016, Chandragiri *et al.* reported the magnetic behavior of polycrystalline  $\text{Gd}_3\text{Ru}_4\text{Al}_{12}$ , the magnetic susceptibility of which follows the Curie-Weiss law above 200 K and of which the Curie-Weiss temperature ( $\theta_p$ ) is estimated to be +80 K [11]. The magnetic susceptibility begins to increase rapidly as the temperature is lowered below 50 K, which implies the development of an FM correlation between spins. However, it exhibits a sharp peak at 18.5 K, indicating an AFM order. The magnetic susceptibility exhibits a very small difference under zero field cool (ZFC) and field cool (FC) conditions, whereas the magnetic specific heat exhibits a broad maximum near 50 K, as if it were a glassy ground state. The behavior of the magnetic susceptibility under magnetic fields mimics that is expected for the Griffiths phase [12]. In 2018, we investigated the low-temperature magnetic and thermodynamic properties of single-crystalline  $\text{Gd}_3\text{Ru}_4\text{Al}_{12}$  [13]. We proposed that FM spin trimers are formed on small Gd triangles, and that the distorted Kagome lattice of  $\text{Gd}_3\text{Ru}_4\text{Al}_{12}$  effectively transforms into an antiferromagnetic triangular lattice (AFMTL), which induces geometrical frustration at low temperatures. The blue arrows labeled  $S_r$  in Fig. 1 denote the resultant spin ( $S_r = 21/2$ ) formed by the Ruderman–Kittel–Kasuya–Yosida (RKKY) interaction with trimers. This  $S_r$  begins to form at approximately 150 K and is completed below 70 K. The binding energy is believed to be 184 K per Gd ion [13]. As the temperature further decreases,  $\text{Gd}_3\text{Ru}_4\text{Al}_{12}$  exhibits successive AFM phase transitions at  $T_2 = 18.6$  K and  $T_1 = 17.5$  K. The magnetic entropy at  $T_2 = 18.6$  K is only 40% of  $R\ln 8$ , indicating the formation of trimers. Because the binding energy is much higher than these transition temperatures, the FM trimers may be stable even in the ordered phases.

\*Corresponding author: shintaro.nakamura.c8@tohoku.ac.jp

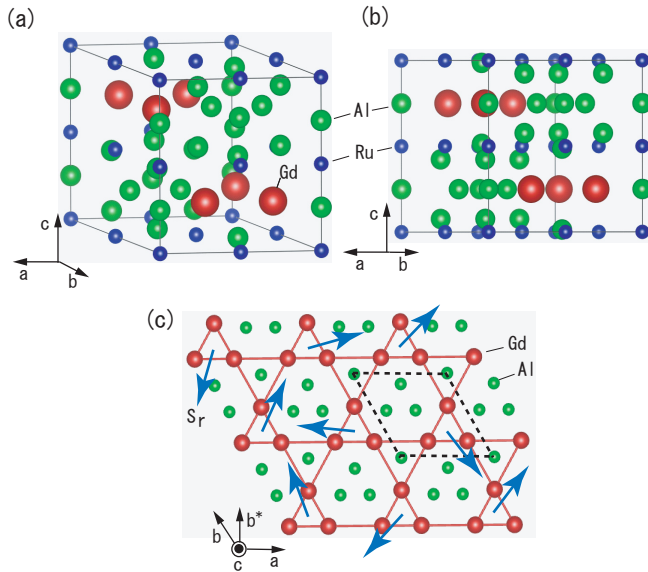


FIG. 1. (a) Structure of  $\text{Gd}_3\text{Ru}_4\text{Al}_{12}$  [1,2]. The red (large), blue (small), and light-green (medium-sized) spheres denote Gd, Ru, and Al ions, respectively. (b) Structure projected parallel to the  $ab$  plane. (c) A Gd–Al layer projected parallel to the  $c$  axis. The red (larger) and light-green (smaller) spheres denote Gd and Al ions, respectively. Bonds are drawn between the nearest neighbor and the next-nearest neighbor of the Gd ions. The blue arrows indicate the resultant spin  $S_r$  ( $S_r = 21/2$ ) on the FM trimers. The broken rhombus indicates a unit cell. The arrow  $b^*$  denotes the direction of the reciprocal lattice vector of  $b$ .

In 2019, resonant x-ray diffraction (RXD) measurements were performed on  $\text{Gd}_3\text{Ru}_4\text{Al}_{12}$  by Matsumura *et al.* and Hirschberger *et al.* [14,15]. The formation of FM trimers was supported by these microscopic measurements, and they reported that the  $S_r$ s have a helical structure along the  $a$  axis. Hirschberger *et al.* reported the existence of a skyrmion phase upon exposure to magnetic fields applied along the  $c$  axis [15]. In many cases, skyrmion states are expected in crystals with noninversion symmetry where Dzyaloshinsky-Moriya (DM) interaction stabilize helical spin structures [16,17]. However, the crystal of  $\text{Gd}_3\text{Ru}_4\text{Al}_{12}$  has an inversion symmetry.  $\text{Gd}_3\text{Ru}_4\text{Al}_{12}$  therefore exhibits peculiar magnetic properties; however, the origin of the magnetic anisotropies and the origin of the helical structure have not been clarified. The ground state of  $\text{Gd}^{3+}$  carries only a pure spin. However, once the trimers are formed at much higher temperatures than  $T_N$ , the fundamental magnetic constituent unit is no longer the  $\text{Gd}^{3+}$  ion but the FM trimer. In the present study, we investigated the magnetic properties of  $\text{Gd}_3\text{Ru}_4\text{Al}_{12}$  by using thermodynamical observations, and discuss the relationships among the magnetic anisotropies, magnetic quadrupole moments of the FM trimers and stability of the helical structure.

## II. SAMPLE PREPARATION AND EXPERIMENTAL METHOD

We melted 3N-Gd, 3N-Ru, and 5N-Al in a tetra-arc furnace and pulled a single-crystal ingot. Considering the evaporation loss, the initial weight of Al was increased by 1–2%

compared with the stoichiometric amount. The obtained ingot was approximately 2–3 cm in length and 3 mm in diameter. We determined the crystalline structure of the ingot by performing x-ray diffraction with crushed powder samples. The diffraction pattern was consistent with that of a previous report [1]. The lattice constants of  $\text{Gd}_3\text{Ru}_4\text{Al}_{12}$  were obtained as 0.8778 nm for the  $a$  axis and 0.9472 nm for the  $c$  axis. The length of the side of the small regular triangle was 0.3698 nm, and that of the large regular triangle was 0.5079 nm. We cut three crystal samples from the ingot, one for magnetization measurements of 29.55 mg, the other one for specific heat measurements of 7.76 mg respectively. Both samples were the same as those used in the previous investigation [13].

The samples for magnetization measurements was approximately a rectangular shape. The lengths of the sides were 1.85 mm ( $\parallel a$ ), 1.85 mm ( $\parallel b^*$ ), and 1.70 mm ( $\parallel c$ ). Using a spheroid approximation, the demagnetizing field coefficients were estimated to be  $D_a = 0.32$ ,  $D_{b^*} = 0.32$ ,  $D_c = 0.36$ . Here, we assume that the ratio of the long axis and short axis is 1.85 : 1.70. The sample for specific heat measurements was approximately a rectangular shape of 0.40 ( $\parallel a$ )  $\times$  0.60 ( $\parallel b^*$ )  $\times$  0.52 ( $\parallel c$ )  $\text{mm}^3$ . We assume that the axis of rotation is parallel to the  $c$  axis, and the demagnetizing field coefficients  $D_a = 0.43$ ,  $D_{b^*} = 0.29$ ,  $D_c = 0.29$  were obtained. In the present paper, we present the data as functions of external field. We did not correct the data in consideration of shape effect.

Specific heat measurements were performed by employing a thermal relaxation method using a commercial instrument (PPMS-9, Quantum Design Inc.) above 2 K and a quasadiabatic method with a hand-made instrument below 2 K. The magnetization was measured using two superconducting quantum interference device magnetometers (MPMS, Quantum Design Inc.).

## III. EXPERIMENTAL RESULTS

### A. Magnetic susceptibility and specific heat

The FM trimers ( $S_r = 21/2$ ) in  $\text{Gd}_3\text{Ru}_4\text{Al}_{12}$  are considered to form the AFMTL at low temperatures [13]. We remeasured the magnetic susceptibilities of  $\text{Gd}_3\text{Ru}_4\text{Al}_{12}$  to determine the anisotropic fields. Figure 2 shows the magnetic susceptibilities below 80 K. The results agree well with the previous reports [13]. The magnetic susceptibility is isotropic at high temperatures, but anisotropy is observed below 60 K, at which formation of the trimers is complete. This implies that the magnetic anisotropy is induced by the formation of  $S_r$ . If we consider the demagnetization effect, the internal fields for  $H \parallel c$  is reduced to be 6.3% compared with the internal fields for  $H \parallel a$  or  $H \parallel b^*$  assuming the spheroid approximation (see Sec. II). However, the difference between the magnetic susceptibility for  $H \parallel c$  and  $H \parallel a$  in Fig. 2 is much larger than this. The anisotropy observed in the magnetic susceptibility cannot be explained only by the demagnetization effect.

The temperature dependence of the magnetic susceptibility  $\chi_{b^*}$  ( $H \parallel b^*$ ) of  $\text{Gd}_3\text{Ru}_4\text{Al}_{12}$  is shown in Fig. 3(a). The open circles and crosses, respectively, denote data from ZFC and FC processes in the presence of a magnetic field of 10 mT. Both  $\chi_{b^*}$  exhibit very small differences between the ZFC

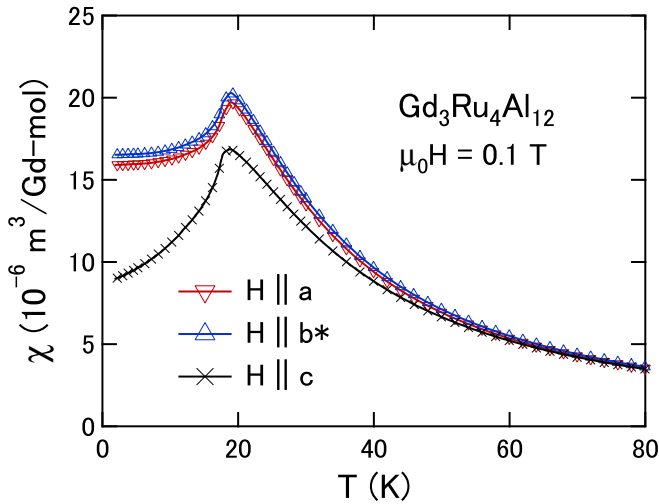


FIG. 2. Temperature dependence of magnetic susceptibility of  $\text{Gd}_3\text{Ru}_4\text{Al}_{12}$ . The applied field is 0.1 T, and the measurements were performed under FC process commonly.

and FC processes. Because the applied magnetic field is very weak, these results include errors of a few percent in the absolute values. The upward arrows in Fig. 3(a) indicate phase transition points. Figure 3(b) shows the second derivatives of  $\chi_{b^*}$  relative to the temperature. We identify the bending points in  $\chi_{b^*}$  as the transition points. The weak anomalies shown in Fig. 3(b) at 12 K are due to the conversion of the thermocouple in MPMS, and are not essential. In this paper, we refer to the lower and higher transition temperatures as  $T_1$  and  $T_2$ , respectively. These transition temperatures are consistent with the previous results [13–15].

The selected temperature dependence of the magnetic susceptibility  $M/H$  at several fields is presented in Fig. 4, where  $T_1$  and  $T_2$  are indicated throughout by the red dotted and blue-solid lines, respectively. Figure 4(a) shows the variation in  $M/H$  at different magnetic field strengths directed along the  $a$  axis. The measurements were performed during the FC processes and we identified the bending points of  $M/H$  as the phase transition points. The application of these fields along the  $a$  axis results in the formation of an intermediate temperature (IMT) phase, which only appears between  $T_1$  and  $T_2$  in the low-field range.

The magnetic susceptibility  $M/H$  measurements by varying the strength of the magnetic field directed along the  $b^*$  axis are presented in Fig. 4(b). The measurements were performed during FC processes. The application of a field along the  $b^*$  axis leads to the appearance of the IMT phase even in the high-field range. As evident in Fig. 4(b), one of the characteristic features of the IMT phase is the weak temperature dependence of  $M/H(T)$ . In other words,  $M/H$  behaves as a transverse susceptibility in the phase.

Figure 4(c) presents the selected magnetic susceptibility  $M/H$  at various fields directed along the  $c$  axis. The measurements were carried out during successive FC and field heat (FH) processes at 0.5, 0.7, 0.8, 1, 1.2, 1.3, 1.8, and 2.5 T, and during the FC process at 3 and 3.5 T. When the field is directed along the  $c$  axis,  $M/H(T)$  exhibits hysteresis loops at  $T_1$  in the range  $0.3 \leq \mu_0 H \leq 1$  T. We identified the bending

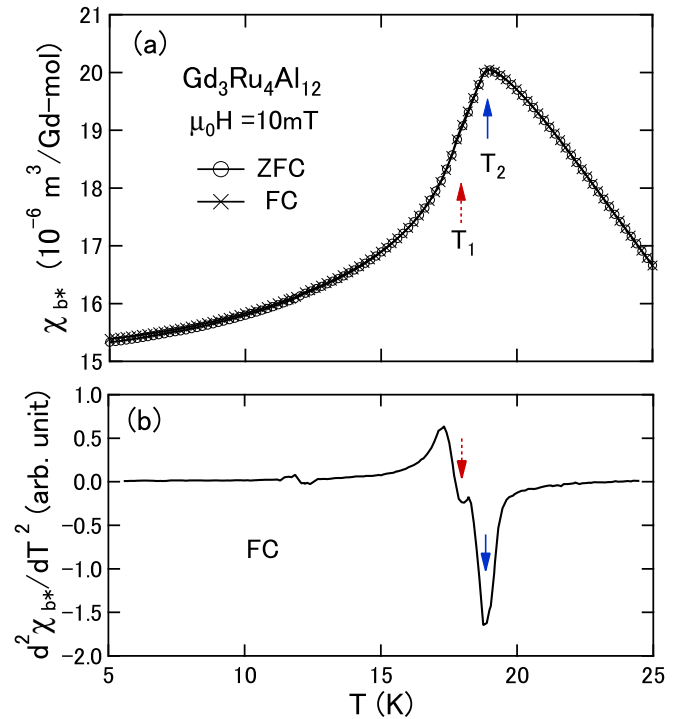


FIG. 3. (a) Temperature dependence of magnetic susceptibility  $\chi_{b^*}$ . The open circles and crosses denote  $\chi$  measured under ZFC (5  $\rightarrow$  25 K) and FC (25  $\rightarrow$  5 K) processes in a presence of a magnetic field of 10 mT. The field is directed along  $b^*$ . The dotted-red and solid-blue upward arrows indicate the phase transition temperatures. The strengths of the fields include errors of a few percent. (b) Second derivative of  $\chi_{b^*}$  (FC) with respect to temperature. The dotted-red and solid-blue downward arrows correspond to bending points in  $\chi_{b^*}$ .

points in the  $M/H$  as  $T_2$ , and the centers of the hysteresis loops as  $T_1$ . The bold-green upward arrows denote additional transition points. An intermediate field phase exists for  $\mathbf{H} \parallel c$ . As indicated in Fig. 4(c) by the black upward arrows and the symbol  $T^*$ , small anomalies are observed between  $T_1$  and  $T_2$  in the field range  $0.3 \leq \mu_0 H \leq 1.5$  T. Hirschberger *et al.* found an unidentified phase transition at  $T^*$  [15]. As shown in Fig. 4(c), the IMT phase appears over a wide range of temperatures in the intermediate field range. In this phase,  $M/H$  exhibits a weak temperature dependence, which appears similar to transverse magnetic susceptibility. However, the temperature dependence of  $M/H$  is more pronounced in the low-temperature phase at low fields. Apparently, a component of the longitudinal magnetic susceptibility exists in this phase when the applied field is directed along the  $c$  axis.

The variation in the specific heat  $C$  with the field strength along the  $a$  axis are presented in Fig. 5(a). At low field strengths,  $C$  exhibits clear  $\lambda$ -shaped peaks corresponding to the successive phase transitions at  $T_1$  and  $T_2$ . In the present study, we identified the phase transition points as the points in the middle of the slopes to the right of the peaks. The two peaks that appear at low fields become a single peak as the field strength increases. This behavior of the transition points is consistent with that observed in  $M/H$ , as shown in Fig. 4(a).

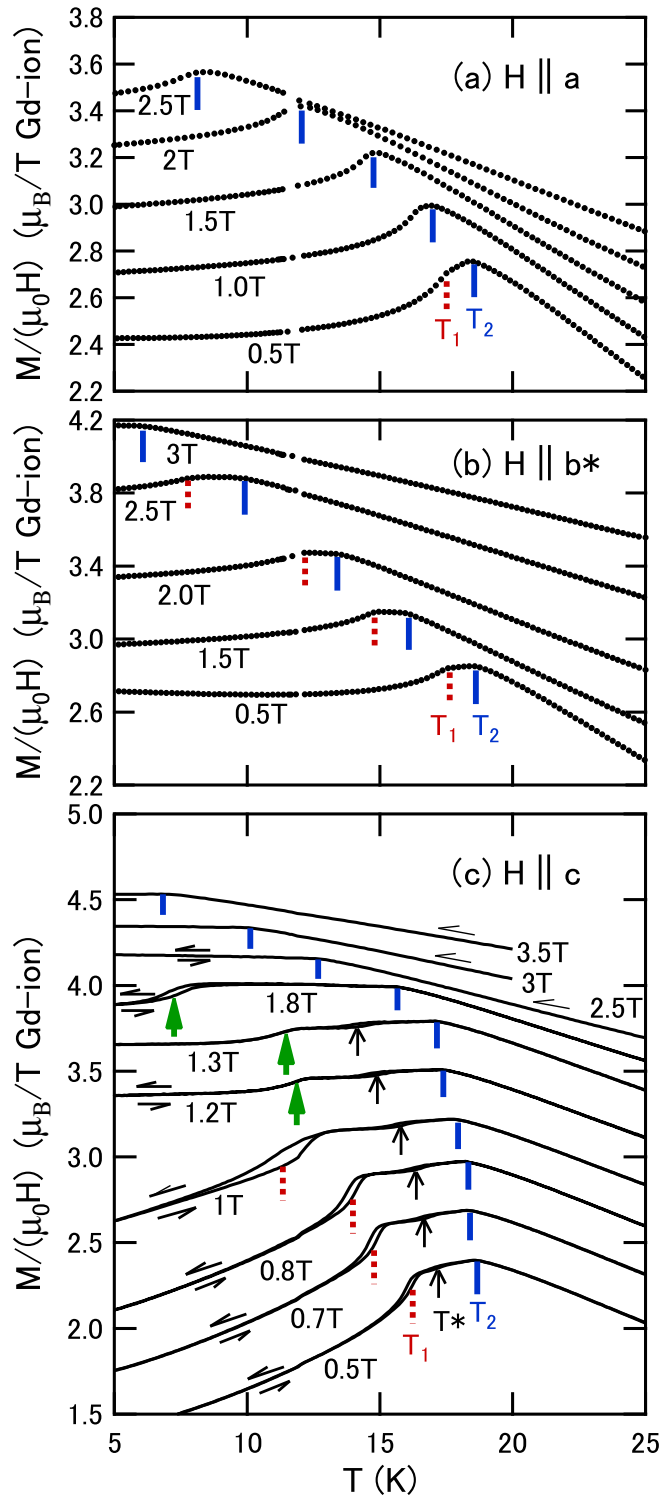


FIG. 4. Phase transition points of  $\text{Gd}_3\text{Ru}_4\text{Al}_{12}$  observed by measuring the temperature dependence of  $M/H$ . The fields are directed along the (a)  $a$  axis, (b)  $b^*$  axis, and (c)  $c$  axis. The red-dotted lines and blue-solid lines indicate  $T_1$  and  $T_2$ , respectively. The bold green arrows in panel (c) indicate other transition points. The origin of each datapoint, except for that at 0.5 T, is shifted in step of (a) 0.3, (b) 0.5, and (c) 0.2  $\mu_B/T$ , respectively, as the field increases. The positioning of the black-thin upward arrows at  $T^*$  is explained in the text.

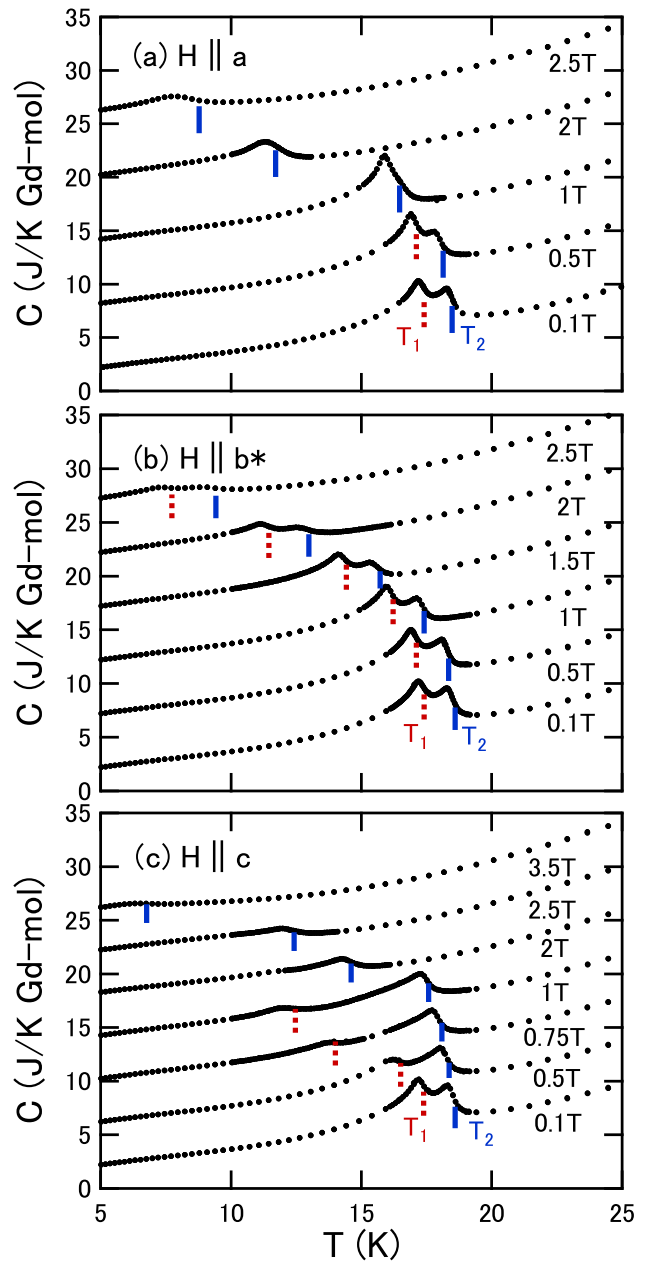


FIG. 5. Phase transition points of  $\text{Gd}_3\text{Ru}_4\text{Al}_{12}$  observed at a specific heat. The fields are directed along the (a)  $a$  axis, (b)  $b^*$  axis, and (c)  $c$  axis. The red-dotted lines and blue-solid lines indicate  $T_1$  and  $T_2$ , respectively. The origin of each set of data, with the exception of 0.1 T, is shifted in step of (a) 0.6, (b) 0.5, and (c) 0.4 J/K Gd-mol, respectively, with increasing fields.

Figure 5(b) shows the specific heat  $C$  when varying the field strength along the  $b^*$  axis are shown. Corresponding to the successive phase transitions at  $T_1$  and  $T_2$ , clear  $\lambda$ -shaped peaks are observed as well. The IMT phase is observed even in high fields, similar to the magnetic susceptibility results presented in Fig. 4(b).

The specific heat  $C$  presented in Fig. 5(c) was measured by varying the strength of the magnetic field directed along



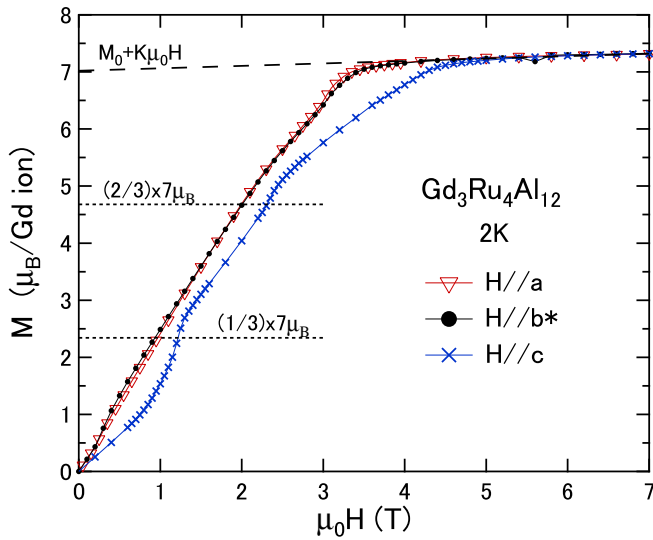


FIG. 6. Magnetization curves of  $\text{Gd}_3\text{Ru}_4\text{Al}_{12}$  at 2 K in a field increasing process. The fields are directed along the  $a$ ,  $b^*$ , and  $c$  axes. The broken line is a fit to the formula  $M(H) = M_0 + K\mu_0H$  in the range  $5.6 < \mu_0H < 7$  T for  $\mathbf{H} \parallel c$ . Here,  $M_0$  is a constant that is independent of the field, and  $K$  is a proportional constant. The dotted lines are guides for the eye denoting  $M = F \times 7\mu_B$  ( $F = 1/3, 2/3$ ).

the  $c$  axis. Clear  $\lambda$ -shaped peaks are observed at  $T_1$  and  $T_2$ . The IMT phase occupies a wide-temperature range in the intermediate-field range. We could not find an indication of the phase transition at  $T^*$  by measuring the specific heat. This seems to suggest that the change in entropy associated with this transition is small.

### B. Magnetization processes

The field dependence of the magnetization  $M$  of  $\text{Gd}_3\text{Ru}_4\text{Al}_{12}$  at 2 K is displayed in Fig. 6. The absolute values of the magnetization contain a few percent error. Overall, the magnetic anisotropy is clearly seen, i.e.,  $\text{Gd}_3\text{Ru}_4\text{Al}_{12}$  is easy to be magnetized when fields are applied in the  $ab$  plane and is hard to be magnetized when fields are applied along the  $c$  axis. A rapid increase in  $M$  is shown at 1.25 T when the field is applied along the  $c$  axis. As shown in Fig. 6, the anisotropy in the  $ab$  plane is very small. The intermediate field phase observed in  $M/H(T)$  was also observed in the range  $1.25 < \mu_0H < 2.4$  T when the field is applied along the  $c$  axis at 2 K. Regardless of the difference in the field direction,  $M$  has a tendency to increase approximately linearly with the magnetic field in the high-field range. In this high-field range, we assume that  $M$  can be described using  $M(H) = M_0 + K\mu_0H$ . Here,  $M_0$  is a constant that does not depend on the field, and  $K$  is a proportional constant. The broken line in Fig. 6 is a fit to the data for  $\mathbf{H} \parallel c$  in the range  $5.6 < \mu_0H < 7$  T. The obtained parameters are  $M_0 = 7.02 \mu_B$  and  $4.3 \times 10^{-2} \mu_B \text{T}^{-1}$ . The magnetization observed exceeds  $7 \mu_B$ , but absolute values measured by the MPMS contain a few percent error. To determine the accurate magnetization processes as field functions, a more precise and wider range of measurement is required. As can be seen in Fig. 6, two rapid increases appear in  $M$  for  $\mathbf{H} \parallel c$  axis at

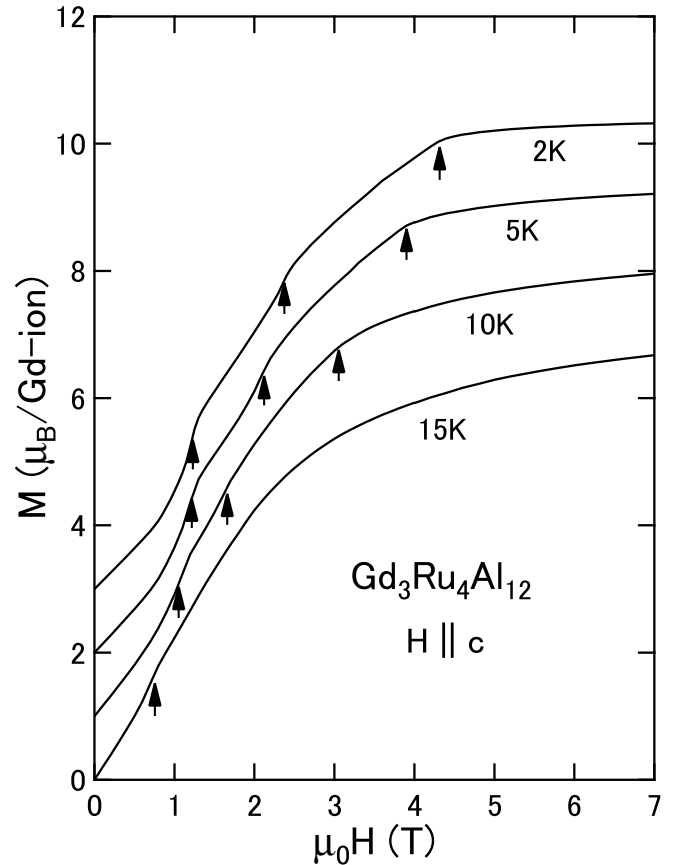


FIG. 7. (a) Data of  $M(H)$  of  $\text{Gd}_3\text{Ru}_4\text{Al}_{12}$  for  $\mathbf{H} \parallel c$  at 2, 5, 10, and 15 K. The arrows indicate the phase transition points. The origin of the left axis is shifted in step of  $1 \mu_B/\text{Gd-ion}$  with decreasing temperature.

approximately 1.25 and 2.4 T. The dotted lines in Fig. 6 denote  $M(H) = F \times 7 \mu_B$ , ( $F = 1/3, 2/3$ ). The rapid increases appear at the points where the magnetization is approximately equal to these values. As shown in Fig. 7, this ratio of magnetization changes with increasing temperature. The lowest transition field is weakly temperature dependent, whereas the temperature dependence of the intermediate transition field is stronger.

Figure 8(a) presents the  $M(H)$  curve for  $\mathbf{H} \parallel a$  at 5 K. The blue downward arrow indicates a phase transition point at 2.86 T. Here, we regard the reflection point as the phase transition point. Figure 8(b) shows the second derivative of  $M$  in Fig. 8(a) with an increasing field process. The arrow in the figure indicates the local minimum point of the second derivative and corresponds to the phase transition point.

Figure 8(c) shows the  $M(H)$  curve for  $\mathbf{H} \parallel b^*$  at 5 K, and Fig. 8(d) shows the second derivative of  $M$  in Fig. 8(c). The red arrows at the lower field side and blue arrows at the higher field side indicate the phase transition points at 2.82 T and 3.06 T, respectively. The minimum points on the second derivative of  $M$  are indicated in Fig. 8(d) and correspond to the transition points in Fig. 8(c). When the fields are directed along the  $b^*$  axis, the intermediate field phase is observed at 5 K.

Figure 9 displays the magnetization curves in the presence of magnetic fields directed along the  $c$  axis. The solid

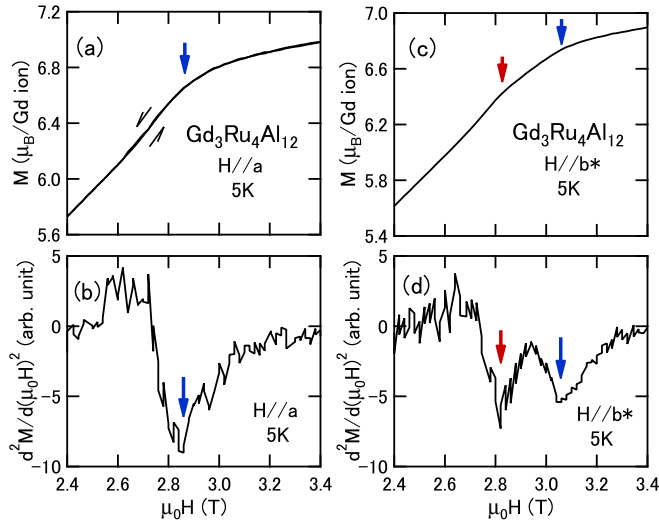


FIG. 8. (a)  $M(H)$  of  $\text{Gd}_3\text{Ru}_4\text{Al}_{12}$  for  $\mathbf{H} \parallel a$  at 5 K. (b) Second derivative of  $M$  in panel (a) with the elevating field process. (c)  $M(H)$  of  $\text{Gd}_3\text{Ru}_4\text{Al}_{12}$  for  $\mathbf{H} \parallel b^*$ . (d) Second derivative of  $M$  in panel (c). The arrows indicate the phase transition points.

downward blue arrows in Fig. 9(a) indicate a phase transition that occurs at high fields. The magnetization curves in the intermediate-field range exhibit small hysteresis loops, as shown in Fig. 9(b). The upward red arrows indicate phase transition points, and the hysteresis loops imply that this transition is of the first order. Similar small hysteresis loops are shown in the low-field range, as shown in Fig. 9(c). The black-bold arrows indicate the phase transitions. In addition, the hysteresis loops imply that this phase transition is first order as well. The additional phase is observed in the intermediate-field range when fields are directed along the  $c$

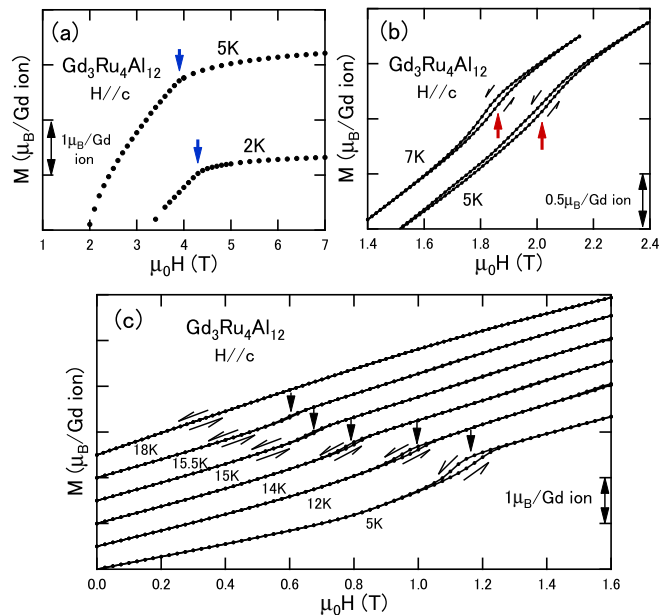


FIG. 9.  $M(H)$  of  $\text{Gd}_3\text{Ru}_4\text{Al}_{12}$  for  $\mathbf{H} \parallel c$  at several temperatures.  $M(H)$  in the (a) high-field, (b) intermediate-field, and (c) low-field ranges. The arrows indicate the phase transition points.

axis, which is the hard axis of magnetization. This suggests that the additional phase is induced with spin flopping.

### C. Magnetic phase diagrams

The magnetic phase diagrams of  $\text{Gd}_3\text{Ru}_4\text{Al}_{12}$  (Fig. 10) could be drawn by analyzing the magnetic susceptibility measurements, magnetization processes, and specific heat results. We refer to the low-temperature and IMT phases as phase I and phase II, respectively, and the intermediate-field phase appears in the fields directed along the  $c$  axis as phase III. The entire view of the magnetic phase diagrams presented in Fig. 10 is anisotropic for Gd compounds. For  $\mathbf{H} \parallel b^*$ , IMT phase II appears in the phase diagram of  $\text{Gd}_3\text{Ru}_4\text{Al}_{12}$ , and is also shown in Fig. 10(b). The boundaries of phase I/phase II and phase II/PM phase display double lines that do not cross.

When the field is applied along the  $c$  axis, as shown in Fig. 10(c), phase III appears between phase I and phase II in the intermediate-field range, and phase II occupies a relatively wide region in the diagram. As mentioned before, the magnetization exhibits hysteresis at the phase I/phase III and phase III/phase II transition points, and therefore, both of these transitions are of the first-order. Hirschberger *et al.* reported the existence of a skyrmion lattice phase and non-identified phase V, respectively, in the regions of phase III and phase II in Fig. 10(c) [15]. In the present study, under the premise that the existence of these phases was observed by microscopic measurements, we focus on the characteristic appearance of the magnetic phase diagrams in their totally, as determined by macroscopic measurements.

The phase diagrams in Fig. 10 look like a superposition of two non-frustrated AFM spin systems, as depicted in Fig. 11. In this figure, the first of these system is the AFM spin system ( $T_N = T_2$ ) that has an easy plane (the  $ab$  plane)-type anisotropy, and the other ( $T_N = T_1$ ) has an easy axis (the  $c$  axis)-type anisotropy. The easy plane-type spin system exhibits a simple single phase boundary regardless of the direction in which the fields are applied. Here, the in-plane anisotropy is assumed to be weak. The easy axis-type spin system shows a spin-flopping-like transition when fields are applied along the  $c$  axis. The only exception to this view is the boundary depicted by the broken line in Fig. 11. This is understandable if we assume that phase II is a partially disordered phase, and phase I is a fully ordered phase. The fully ordered phase appears as a lower-temperature phase in relation to a partial ordered phase, but the reverse situation is impossible. Different types of anisotropies would seem to coexist in  $\text{Gd}_3\text{Ru}_4\text{Al}_{12}$ . The dotted line in Fig. 10(c) corresponds to the weak anomalies at  $T^*$ , as shown in Fig. 4(c).

## IV. DISCUSSION

### A. Magnetic fields with two types of anisotropies

In this section, we estimate the magnitude of the anisotropic energies. The magnetic susceptibility in Fig. 4 and magnetization process in Fig. 6 indicate the easy-axis-type of anisotropy, whereas the magnetic phase diagrams in Fig. 10 imply the coexistence of different anisotropies. The magnetic susceptibilities in Fig. 2 at low temperatures are replotted

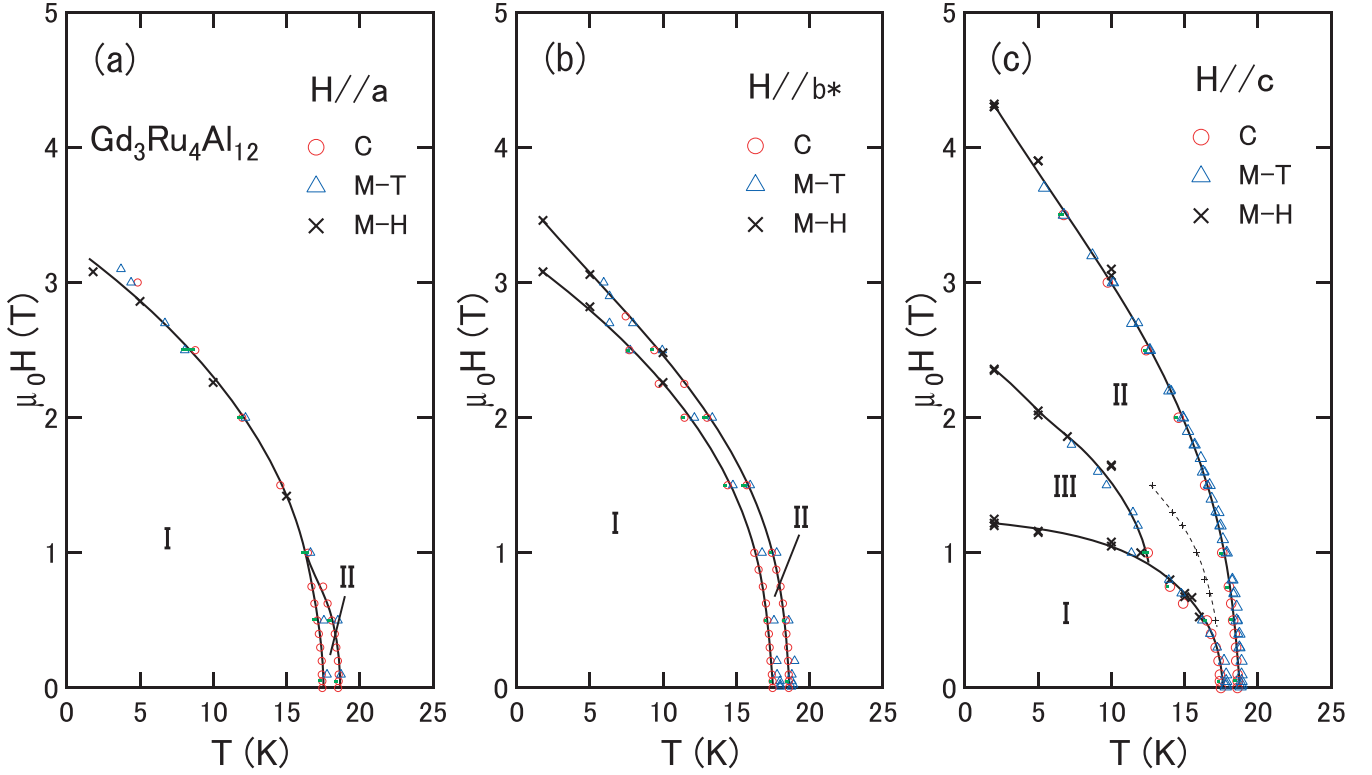


FIG. 10. Magnetic phase diagrams of  $\text{Gd}_3\text{Ru}_4\text{Al}_{12}$  for the (a)  $\mathbf{H} \parallel a$ , (b)  $\mathbf{H} \parallel b^*$ , and (c)  $\mathbf{H} \parallel c$  axes. The red circles, blue triangles, and black crosses indicate phase transition points determined from the specific heat and  $M/H(T)$  and  $M(H)$  measurements, respectively. Data for  $C$  at zero field were taken from the reference [13]. The dotted line in the right panel corresponds to  $T^*$ , as shown in Fig. 4(c). The horizontal-green line segments denote transition temperature errors estimated from Fig. 5. Each length of the line segment corresponds to the difference between the temperature at the mid point of the right-side slope of the specific heat and that at the peak of the specific heat.

in Fig. 12 on expanded scales. In this figure, the magnetic susceptibilities are plotted as a function of  $T^2$ . Here, AFM spin waves are expected to contribute to the magnetization at finite temperatures. According to previous theories based on spin wave approximation, the contribution of the AFM spin waves propagating in three dimensions can be expressed as  $M(T) - M(0) \propto T^2$  for isotropic systems [18–20] and  $M(T) - M(0) \propto T^{1.5} \exp[-(k_B^{-1}E_g)/T]$  for anisotropic systems [20] when the temperatures are sufficiently lower than the Néel temperature. Here,  $M(0)$  is the magnetization at 0 K

and  $E_g$  is the energy gap in the AFM magnon dispersion

$$E_g = \hbar\Omega = \hbar\sqrt{\omega_A^2 + 2\omega_{ex}\omega_A}, \quad (1)$$

where  $\Omega$  has the lowest precession frequency of magnons,  $\hbar\omega_A = 2\mu_B S_r H_A$  is the crystal magnetic anisotropic energy of a single trimer, where  $H_A$  represents the anisotropic fields. In addition,  $\hbar\omega_{ex} = 2JS_r z$  is the exchange energy owing to the exchange interactions from the nearest-neighbor  $S_r$  of number  $z$ . When the applied external field is sufficiently weak,  $M$  can be replaced by the molar magnetic susceptibility  $\chi$  as follows:

$$\chi(T) - \chi(0) = C_1 T^2 \quad (2)$$

for an isotropic system, and

$$\chi(T) - \chi(0) = C_2 T^{1.5} \exp[-(k_B^{-1}E_g)/T] \quad (3)$$

for an anisotropic system. Here,  $C_1$  and  $C_2$  are proportional constants.

First, we estimate the energy gap of the magnon. The solid blue and red curved lines in Fig. 12 correspond to Eq. (3). The calculated data well reproduce the experimentally observed  $\chi_a$  and  $\chi_{b^*}$ . The  $k_B^{-1}E_g$  values obtained are 25 K for  $\chi_a$  and 30 K for  $\chi_{b^*}$ , being approximately isotropic in the  $ab$  plane. The temperature dependence of  $\chi_a$  and  $\chi_{b^*}$  can be understood as the contribution from spin waves (waves of  $S_r$ s) propagating in three dimensions under easy-plane-type anisotropic fields  $\mathbf{H}_A^{pl}$ . Here, the directions of  $S_r$ s are in the  $ab$  plane, and the polarization of the waves is vertical to the  $ab$  plane. The

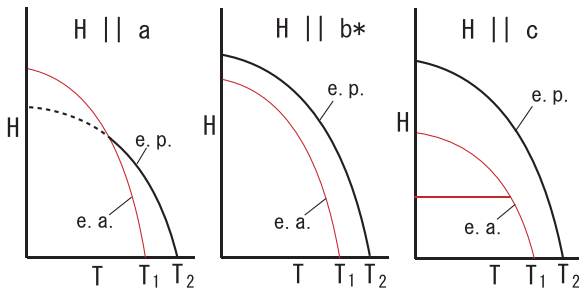


FIG. 11. Superposition of schematic phase diagrams of nonfrustrated AFM material with an easy-plane ( $ab$  plane)-type anisotropy ( $T_N = T_2$ ) and that with an easy-axis ( $c$  axis)-type anisotropy ( $T_N = T_1$ ). The broken line is the boundary, which is not observed in actual  $\text{Gd}_3\text{Ru}_4\text{Al}_{12}$  owing to the frustration (see text).

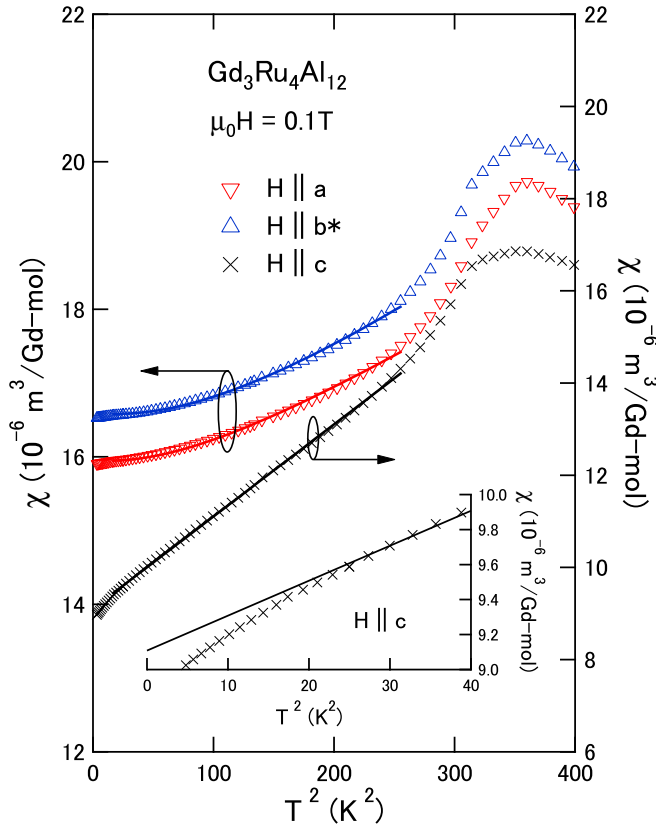


FIG. 12. Temperature dependence of the magnetic susceptibility of  $\text{Gd}_3\text{Ru}_4\text{Al}_{12}$ . The data were obtained from Fig. 2 and were replotted on a  $T^2$  scale. The applied field is 0.1 T. The solid-curved lines are fits to Eq. (3), and the solid-straight line is a fit to Eq. (2). These lines also indicate the fitting regions. The magnetic susceptibility for  $\mathbf{H} \parallel \mathbf{c}$  is presented in the inset on expanded scales. The fitting line is expanded to the zero temperature in the inset.

resultant spin  $\mathbf{S}_r$ s that are directed in the  $ab$  plane are under easy-plane-type anisotropic fields, and the energy gap of the magnon is estimated to be 25–30 K.

Next we discuss the phase transition by the applied field, which is directed along the  $c$  axis. As shown in Fig. 6, discontinuous change in magnetization is observed at 1.3 T when field is applied along the  $c$  axis. According to the previous RXD, this change in magnetization corresponds to the transition from the helical structure to a conical structure of  $\mathbf{S}_r$  [14,15]. The observed propagation vector is  $k = 0.27$  along the  $a$  axis. Here, we consider two kinds of  $\mathbf{S}_r$  structures shown in Fig. 13. For simplicity, we approximate the propagation vector to  $k = 0.25$ . Figure 13(a) shows a helical structure and Fig. 13(b) shows a spiral structure in which all  $\mathbf{S}_r$ s are directed in the  $ab$  plane. When weak field  $H_a$  is applied along the  $c$  axis, the  $\mathbf{S}_r$  structures in Fig. 13(a) and Fig. 13(b) change into structures in Fig. 13(c) and Fig. 13(d), respectively. Energies of the systems in Figs. 13(c) and 13(d) per unit volume are expressed as

$$E_j(H_a) = E_j(0) - (1/2)\mu_0\mathbf{H}_a \cdot \mathbf{M}_j(H_a), \quad (j = c, d). \quad (4)$$

Here,  $\mathbf{M}_j(H_a)$  is the magnetization per unit volume induced by  $\mathbf{H}_a$ . As shown in the inset of Fig. 14,  $\mathbf{S}_r$ s, which are directed in the  $ab$  plane in Figs. 13(a) and 13(b) are canted

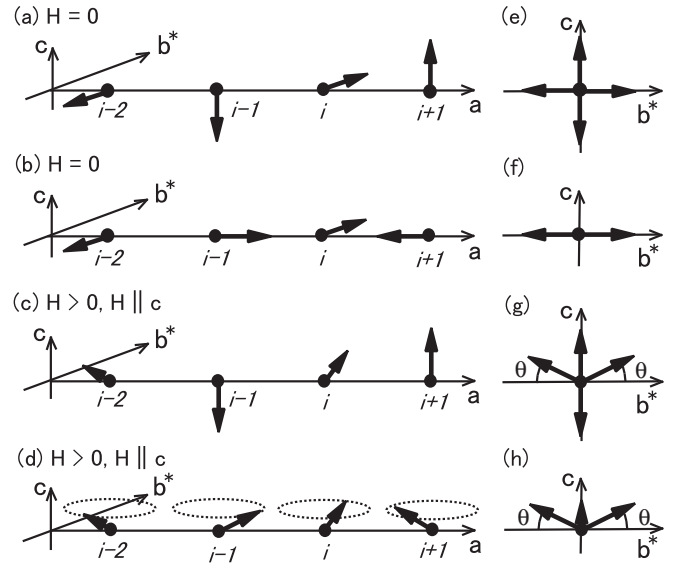


FIG. 13. Two types of structures of  $\mathbf{S}_r$ . (a) The helical structure of  $\mathbf{S}_r$  along the  $a$  axis with propagation vector  $k = 0.25$  at zero field. (b) The spiral structure of  $\mathbf{S}_r$  along the  $a$  axis with propagation vector  $k = 0.25$  at zero field. Directions of  $\mathbf{S}_r$  are in the  $ab$  plane. (c) The structure (a) modulated by a weak field along the  $c$  axis. (d) The structure (b) modulated by a weak field along the  $c$  axis. [(e)–(h)] Projection drawings of (a)–(d) along the  $a$  axis, respectively.

by  $\mathbf{H}_a$  and magnetization directed along the  $c$  axis is induced. On the other hand,  $\mathbf{S}_r$ s, which are directed in the  $c$  axis Fig. 13(b) do not change the direction therefore do not contribute the magnetization. The solid curves in Fig. 14 are field dependence of  $E_j(H_a)$ , ( $j = c, d$ ). In this figure,  $E_d(0)$  and  $\Delta_A$  are defined as zero and  $E_d(0) - E_c(0)$ , respectively.  $N_{S_r}$  is the number of  $\mathbf{S}_r$  in unit volume. If we assume that the  $\Delta_A$  is an easy-axis-type anisotropic energy, which works on  $\mathbf{S}_r$ s directed along the  $c$  axis, the transition from helical [Fig. 13(c)] to conical structure [Fig. 13(d)] is expected at

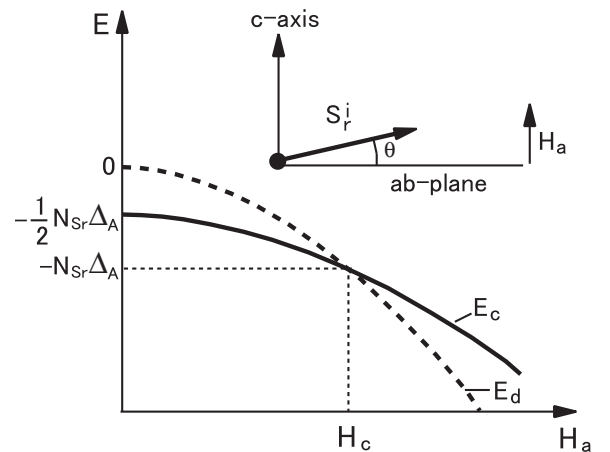


FIG. 14. Field dependence of energies of the  $\mathbf{S}_r$  structures in Fig. 13. As shown in Fig. 13,  $\mathbf{S}_r^i$  is parallel to the  $ab$  plane at zero field. Applied field is directed along the  $c$  axis. The solid and broken curves denote the energies  $E_c$  and  $E_d$  of Eq. (4), respectively.  $H_c$  is the transition field. The inset shows the  $\mathbf{S}_r^i$  canted by the field  $\mathbf{H}_a \parallel \mathbf{c}$ .



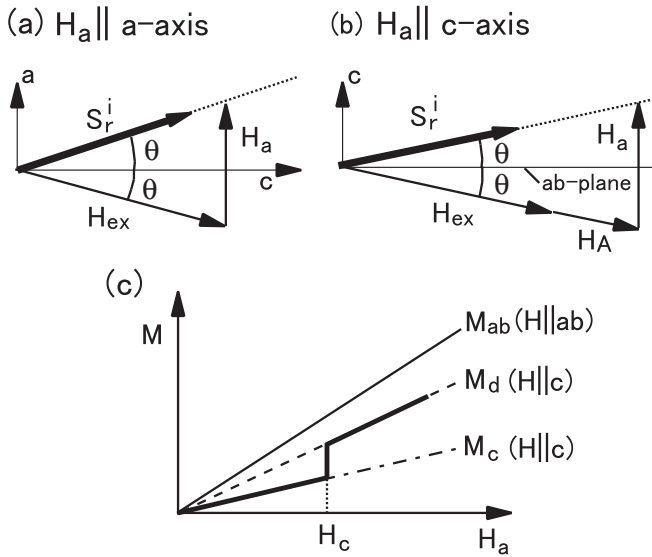


FIG. 15. (a) Tilted  $S_r^i$  in Fig. 13(a) when  $H_a$  is applied along the  $a$  axis. Here,  $H_{ex}$  is the exchange dipole field. (b) Tilted  $S_r^i$  when  $H_a$  is applied along the  $c$  axis, where  $H_{ex}$  is the exchange dipole field and  $H_A$  is the effective anisotropic field of easy-plane type originating from the magnetic quadrupole interaction. (c) Magnetization process in the low field range. Here,  $M_c$  (dotted-broken line) and  $M_d$  (broken line) denote the magnetization process of the spin structure in Figs. 13(c) and 13(d), respectively. The bold-zigzag line indicates the actual magnetization process when the field is applied along the  $c$  axis.  $H_c$  is the transition field from the helical structure [Fig. 13(c)] to the conical structure [Fig. 13(d)].  $M_{ab}$  is the magnetization process when  $H_a$  is applied parallel to the  $ab$  plane.

$H_c$ . Figure 15 displays the aspect of  $S_r^i$  and  $M$  in the vicinity of  $H_c$ . The discontinuous increase in  $M$  is expected at  $H_c$ . The easy-axis-type anisotropic energy stabilize the helical structure at fields lower than  $H_c$ .

We estimate the anisotropic fields, which act on  $S_r$ s directed along the  $c$  axis. The solid-black straight line in Fig. 12 is fitted by Eq. (2). The calculated values are in good agreement with the experimentally observed  $\chi_c$ . The spin waves excited in  $S_r$ s, which are directed along the  $c$  axis, are polarized vertically to the  $c$  axis, and they propagate under weak anisotropic fields. As is evident from the inset in Fig. 12,  $\chi_c$  deviates from the fit below 5 K. This implies that the anisotropic energy  $k_B \Delta_A$  is approximately 5 K. As shown in Fig. 6, a jump occurs in the magnetization at 1.3 T. The jump in the magnetization at approximately 1.3 T in Fig. 7 becomes less prominent at temperatures higher than 5 K. Therefore, the anisotropic energy of the easy-axis type is estimated to be approximately 5 K. We examined these estimations from the another point of view. The induced magnetic moment of single  $S_r$  at  $H_c = 1.3$  T is obtained to be  $7.2 \mu_B$  per  $S_r$  as shown in Fig. 6. Therefore,  $k_B \Delta_A$  is approximately 6.2 K, and this agrees with the obtained values mentioned above.

Here, we examine the consistency of the obtained anisotropic energy and magnetic phase diagrams, and estimate the anisotropic energy of the easy-plane type. When fields are applied along the  $c$  axis, the anisotropic fields  $H_A^{pl}$  that are parallel to the  $ab$  plane resist changes in the directions

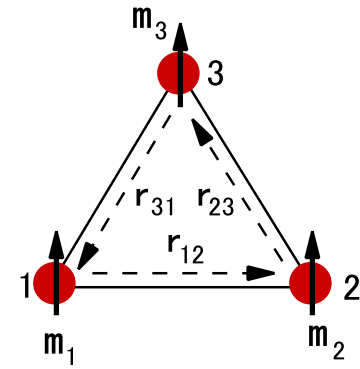


FIG. 16. Magnetic moments  $m_i$  ( $m_i = 7\mu_B$ ) on a FM trimer. Here, the subscripts  $i = 1, 2, 3$  denote the vertices of the triangle. The red spheres indicate Gd ions. The vector  $r_{ij}$  denotes the position of vertex  $j$  relative to that of vertex  $i$ .

of  $S_r$ , and stabilize the AFM phase as a result. However, when fields are applied parallel to the  $ab$  plane,  $H_A^{pl}$  does not contribute to the stability of the AFM phase, because it is isotropic in the  $ab$  plane. In fact, the phase II/PM phase transition field for  $H \parallel c$  at 1.8 K is increased by 0.86 T when compared with that obtained for  $H \parallel b^*$  at 1.8 K (see Fig. 10). Therefore,  $\mu_0 H_A^{pl}$  would be approximately 0.86 T, and this gives  $k_B^{-1} \hbar \omega_A \simeq 12$  K. On the other hand, the exchange energy  $k_B^{-1} \hbar \omega_{ex}$  in Eq. (1) is approximately equal to  $T_2 = 18.6$  K. Substituting  $k_B^{-1} \hbar \omega_{ex}$  and  $k_B^{-1} \hbar \omega_A$  into Eq. (1),  $k_B^{-1} E_g \simeq 24$  K is obtained. This is in approximate agreement with that obtained from the analysis of  $\chi(T)$ . Therefore, the anisotropic energy of the easy-plane type was estimated to be 12 K. Consequently, the present results indicate that there are different anisotropic fields in  $Gd_3Ru_4Al_{12}$  depending on the directions of  $S_r$ s. The first is the strong easy-plane-type anisotropic field, and the other is the weak easy-axis-type field.

### B. Origin of the anisotropic magnetic fields

In this section, we consider the origin of the unusual anisotropic magnetic fields in  $Gd_3Ru_4Al_{12}$ . A possible origin of the anisotropy to be examined is electromagnetic interaction. Figure 16 displays an FM trimer on which three magnetic moments  $m_i$  ( $i = 1, 2, 3$ ;  $m_i = 7\mu_B$ ) are placed. Here, the subscripts  $i = 1, 2, 3$  indicate the number of vertices, and  $\mu_B$  is the Bohr magneton. The vector  $r_{ij}$  denotes the position of vertex  $j$  relative to that of vertex  $i$ . The flux density  $B_{ij}$  at vertex  $j$  induced by  $m_i$  at vertex  $i$  is given by

$$B_{ij} = -\frac{\mu_0}{4\pi r^3} \left[ m_i - \frac{3(m_i \cdot r_{ij})r_{ij}}{r^2} \right].$$

When the FM trimer is formed at low temperatures, all three magnetic moments are written as  $m$ . Therefore, the electromagnetic energy of the trimer is

$$E_{em} = \frac{\mu_0}{4\pi r^3} \left[ 3m^2 - 3 \sum_{ij} \frac{(m \cdot r_{ij})^2}{r^2} \right]$$

at a unit of J per  $S_r$ , where the suffix takes the values ( $ij = 12, 23, 31$ ). This energy becomes the lowest when  $m$

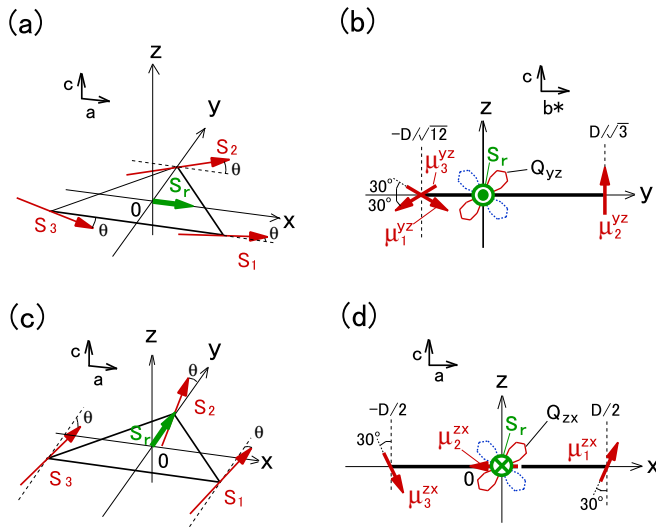


FIG. 17. Ferromagnetic spin trimers of  $\text{Gd}_3\text{Ru}_4\text{Al}_{12}$  with imperfection of directivity. The coordinates  $x$ ,  $y$ , and  $z$  are taken parallel to the  $a$ ,  $b^*$ , and  $c$  axes, respectively. The origin is taken at the center of gravity of the triangle. The bold-green arrows and symbols  $\otimes$  and  $\odot$  indicate the directions of  $S_r$ s. (a) Trimer of which the  $S_r$  is directed along the  $x$  axis. Each component spin  $S_i$  ( $i = 1, 2, 3$ ) forms an angle  $\theta$  with respect to the  $z$  axis.  $D$  is the length of the small triangle side. (b) Projected drawing of the trimer in panel (a) parallel to the  $x$  axis. The magnetic moments  $\mu_i^{yz}$  ( $i = 1, 2, 3$ ) are in- $yz$ -plane components. The curves with the four-leaf-clover shape represent the magnetic quadrupole moment  $Q_{yz}$ . (c) Trimer of which the  $S_r$  is directed along the  $y$  axis. Each component spin  $S_i$  ( $i = 1, 2, 3$ ) forms an angle  $\theta$  with respect to the  $y$  axis. (d) Projected drawing of the trimer in panel (c) parallel to the  $y$  axis. The magnetic moments  $\mu_i^{zx}$  ( $i = 1, 2, 3$ ) are in- $zx$ -plane components of component spins  $S_i$  ( $i = 1, 2, 3$ ). The curves with four-leaf-clover shape represent the magnetic quadrupole moment  $Q_{zx}$ .

is directed in the  $ab$  plane. The electromagnetic energy  $E_{em}$  gives rise to the easy-plane-type anisotropy, and it is isotropic in the  $ab$  plane. However, the amplitude of this energy is approximately 2.7 K per  $S_r$ . This is too small to explain the easy-plane-type anisotropic energy that was observed. Therefore, electromagnetic interaction is not the origin of the anisotropic fields.

Another possible origin of the anisotropic magnetic fields may be magnetic quadrupole interactions according to the RKKY mechanism. The magnetic trimer occupies a much larger area than a single  $\text{Gd}^{3+}$  ion. In this case, we need to consider the effects of magnetic multipole moments and the interactions among them, because multiple moments rapidly enlarge as the size of the trimer increases. Generally, if the FM directivity of the component spins of a trimer were imperfect, the trimer would carry not only dipole moments but also magnetic multipole moments. Actually, the previous RXD measurements indicate the imperfections of directivity in trimers [14]. Here, we assume an FM trimer with an imperfection of directivity as depicted in Fig. 17(a). In this figure, the coordinate axes  $x$ ,  $y$ , and  $z$  are parallel to the  $a$ ,  $b^*$ , and  $c$  axes, respectively. The origin was taken to be located at the triangular center of gravity. As shown in Fig. 17(a), the component spins  $S_i$  ( $i = 1, 2, 3$ ) form the angle  $\theta$  with respect

to the  $x$  axis, and the resultant spin  $S_r$  is parallel to this axis. Figure 17(b) shows a projection of Fig. 17(a) parallel to the  $x$  axis. The red arrows  $\mu_i^{yz}$  ( $i = 1, 2, 3$ ) in this figure denote the in- $yz$ -plane components of the magnetic moments of  $S_i$ s. Under the condition  $\theta \ll 1$ , the magnitude of these magnetic moments are commonly

$$\mu_i^{yz} = 7\mu_B\theta. \quad (5)$$

Calculating the magnetic quadrupole moments with Eqs. (A1)–(A4) (Appendix A), we obtain the quadrupole moment  $Q_{yz}$  of the trimer as summarized in Table I. Figure 17(c) shows the trimer of which the  $S_r$  is directed along the  $y$  axis, and Fig. 17(d) is a projection drawing parallel to the  $y$  axis. The trimer depicted in Fig. 17(d) carries  $Q_{zx}$ . The quadrupole moment of the trimer of which the  $S_r$  is directed in the  $ab$  plane, can be represented by a linear combination of  $Q_{yz}$  and  $Q_{zx}$ . When the direction of  $S_r$  is in the  $ab$  plane, the magnetic quadrupole interaction acts on  $S_r$ s as an effective anisotropic field of the easy-plane type (Appendices A and B).

In Fig. 18, we present three trimers of which the  $S_r$ s are directed along the  $c$  axis ( $z$  axis). The component spins shown in Fig. 18(a) form an angle  $\theta'$  with respect to the  $z$  axis. Figure 18(b) shows the projection of Fig. 18(a). This trimer carries magnetic quadrupole moment  $Q_{xy}$  as summarized in Table I. The trimer in Figs. 18(c) and 18(d) has a magnetic quadrupole moment  $Q_2^z$ , and the trimer in Figs. 18(e) and 18(f) carries magnetic quadrupole moment  $Q_2^0$ , respectively. The quadrupole moments the trimer can have are restricted by the direction of  $S_r$ . The magnitudes of these quadrupole moments are summarized in Table I. We cannot identify the spontaneous quadrupole moment realized among  $Q_{xy}$ ,  $Q_2^z$ , and  $Q_2^0$  from the macroscopic measurements. In this paper, our discussion assumes that  $Q_2^0$  is realized below, because a similar argument would be valid in the case of  $Q_{xy}$  and  $Q_2^z$ . When  $S_r$  on a trimer is directed along the  $c$  axis, it receives no quadrupole interaction from the trimers with  $Q_{yz}$  and  $Q_{zx}$ . Therefore,  $S_r$  directed along the  $c$  axis does not receive effective anisotropic fields of the easy-plane type; instead, it receives effective anisotropic fields of the easy-axis type from the surrounding  $Q_2^0$ s (Appendix B).

Here, we discuss the frustration among magnetic quadrupole moments. We consider two cases: the case wherein geometrical frustration plays a dominant role and that wherein far-near-neighbor frustration plays a dominant role. In Fig. 19(a), three trimers with magnetic quadrupole moments and  $S_r$ s are illustrated. In this figure, all  $S_r$ s are directed in the  $ab$  plane; therefore, the quadrupole moments are described by linear combinations of  $Q_{ps}$  ( $p = yz, zx$ ). The quadrupole interaction among the three quadrupoles is described as

$$H_{QQ}^{pl} = - \sum_{i,j=1,2,3}^{i \neq j} G_6 [\hat{Q}_{yz}(i)\hat{Q}_{yz}(j) + \hat{Q}_{zx}(i)\hat{Q}_{zx}(j)] \quad (6)$$

from Eq. (A5) (Appendix A). Here, assuming that isotropy exists in the  $ab$  plane,  $G_6$  is independent of the combination ( $i, j$ ). When this quadrupole interaction is antiferromagnetic, geometrical frustration is induced among the quadrupole moments in the triangle. This is because the quadrupole moments

TABLE I. Magnetic quadrupole moments carried by the trimers depicted in Figs. 17 and 18, and the directions of  $S_r$ . Here,  $D$ ,  $\theta$ ,  $\theta'$ , and  $\theta''$  are the length and angles defined in these figures.

Trimers	$Q_{yz}$	$Q_{zx}$	$Q_{xy}$	$Q_2^2$	$Q_2^0$	Directions of $S_r$
in Figs. 17(a) and 17(b)	$\frac{7\sqrt{3}}{2}D\theta\mu_B$	0	0	0	0	$\parallel a$
in Figs. 17(c) and 17(d)	0	$\frac{7\sqrt{3}}{2}D\theta\mu_B$	0	0	0	$\parallel b^*$
in Figs. 18(a) and 18(b)	0	0	$7\sqrt{3}D\theta'\mu_B$	0	0	$\parallel c$
in Figs. 18(c) and 18(d)	0	0	0	$7\sqrt{3}D\theta'\mu_B$	0	$\parallel c$
in Figs. 18(e) and 18(f)	0	0	0	0	$\frac{14\sqrt{3}}{3}D\theta''\mu_B$	$\parallel c$

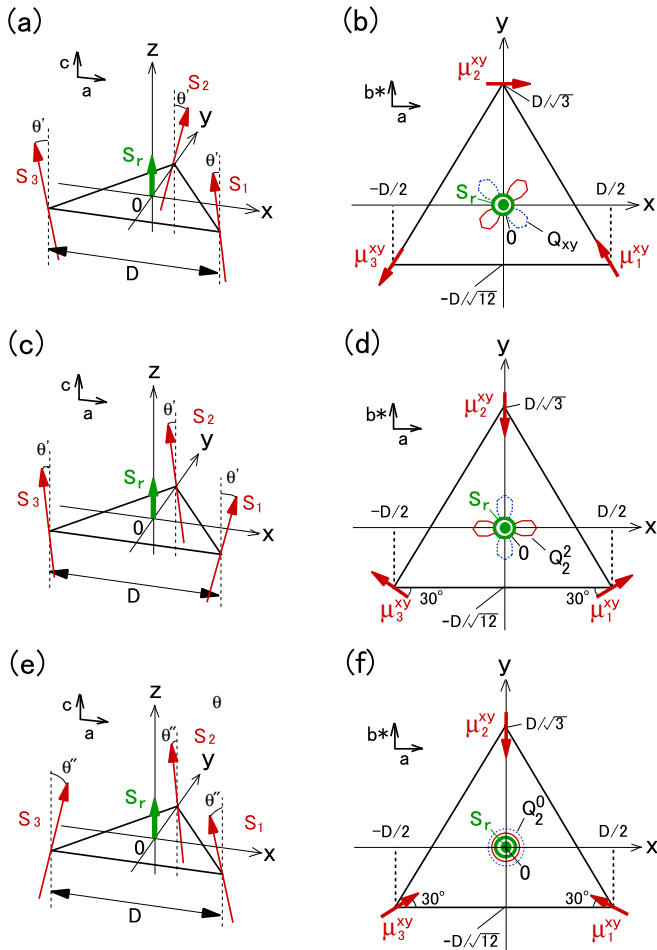


FIG. 18. Ferromagnetic spin trimers of  $Gd_3Ru_4Al_{12}$ , which have imperfection of directivity. The coordinates  $x$ ,  $y$ , and  $z$  are taken parallel to the  $a$ ,  $b^*$ , and  $c$  axes, respectively. The origin is taken at the triangular center of gravity. The bold-green arrows and symbols  $\otimes$  and  $\odot$  indicate the directions of  $S_r$ s. (a) The red-thin arrows denote the component spins  $S_i$ , which form an angle  $\theta'$  with respect to the  $z$  axis. (b) Project drawing of panel (a) parallel to the  $z$  axis. The magnetic moments  $\mu_i^{xy}$  ( $i = 1, 2, 3$ ) are in- $xy$ -plane components. The curves with four-leaf-clover shape represents the magnetic quadrupole moment  $Q_{xy}$ . (c) The red-thin arrows denote the component spins  $S_i$ , which form angle  $\theta'$  with respect to the  $z$  axis. (d) The projected drawing of the trimer in panel (c) parallel to the  $z$  axis. The four-leaf-clover shaped lines denote  $Q_2^2$ . (e) The red-thin arrows represent component spins  $S_i$ , which make angle  $\theta''$  with respect to the  $z$  axis. (f) Projected drawing of the trimer in panel (a) parallel to the  $z$  axis. The red and blue concentric circles denote  $Q_2^0$ .

at vertex-3 in Fig. 19(a) undergo quadrupole interactions of different signs with the quadrupole moments at vertexes-1 and 2, respectively. However, when  $S_r$  at vertex-3 changes its direction parallel to the  $c$  axis as illustrated in Fig. 19(b), the quadrupole moment at vertex-3 changes into  $Q_2^0$ . These changes in the quadrupole moments eliminate the frustration among the quadrupole moments because no quadrupole interaction occurs between  $Q_{ps}$  ( $p = yz, zx$ ) and  $Q_2^0$ .

Figure 20(a) shows three trimers aligned along the  $a$  axis. All the  $S_r$ s are directed in the  $ab$  plane, and the quadrupole moments are described by linear combinations of  $Q_{ps}$ s. Here, we assume that the quadrupole interaction between nearest neighbor is ferromagnetic and that between next-nearest neighbors is antiferromagnetic. In this case, the quadrupole moment at vertex-3 in Fig. 20(a) receives quadrupole interactions with different signs from the quadrupole moments at vertexes-1 and 2, respectively, and frustration is induced among the quadrupole moments. However, if  $S_r$  at vertex-2 changes its direction along the  $c$  axis, as illustrated in Fig. 20(b), the quadrupole moment at vertex-2 changes to  $Q_2^0$ , and the quadrupole frustration among the three trimers is eliminated.

In both the frustrated cases mentioned above, trimers are expected to gain in energy in association with the elimination of quadrupole frustration, and this induces the change in the directions of  $S_r$ s, and may assist the formation of the helical structure of  $S_r$ s. In this meaning, the quadrupole interactions may supply the

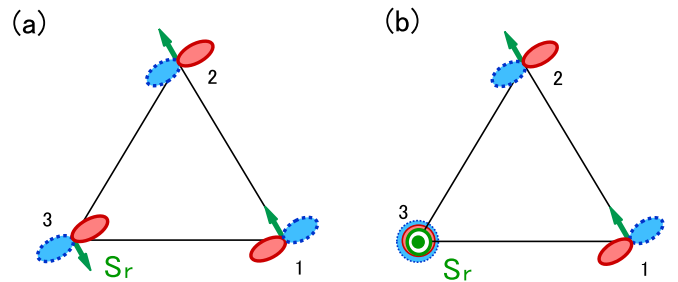


FIG. 19. Trimers with magnetic quadrupole moments on a triangle. (a) All  $S_r$ s at the vertices are directed in the  $ab$  plane. All the quadrupole moments are linear combinations of  $Q_{yz}$  and  $Q_{zx}$ . Antiferroquadrupole interactions among the quadrupole moments induce geometrical frustration. (b)  $S_r$  at vertex-3 denoted by  $\odot$  is directed along the  $c$  axis, and the quadrupole moment at this vertex changes to  $Q_2^0$ , which is depicted as concentric circles colored blue and red. The frustration by AFQ interactions is eliminated.

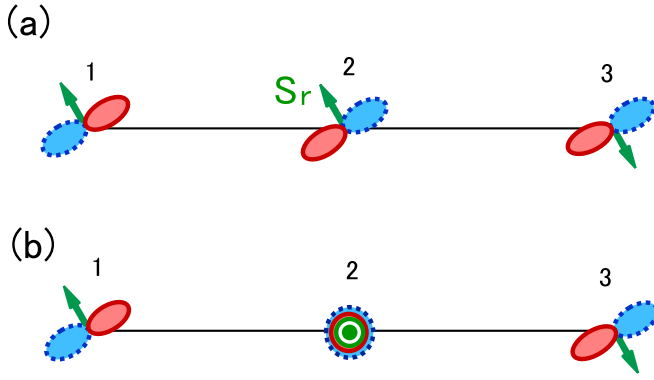


FIG. 20. Trimers with magnetic quadrupole moments on a line. (a) All  $S_r$ s at the vertices are directed in the  $ab$  plane. All quadrupole moments are linear combinations of  $Q_{yz}$  and  $Q_{zx}$ . Ferromagnetic quadrupole interaction between the nearest neighbors and AFM quadrupole interactions between the next-nearest neighbors induce frustration. (b)  $S_r$  at site-2 denoted by  $\odot$  is directed along the  $c$  axis, and the quadrupole moment at this site changes to  $Q_2^0$ , which is depicted as concentric circles in blue and red. The frustration by quadrupole interactions is eliminated.

place of the DM interaction in the inversion-symmetric crystal  $\text{Gd}_3\text{Ru}_4\text{Al}_{12}$ .

### C. Degrees of freedom of magnetic quadrupole moment

Figure 21 shows a trimer that carries three magnetic dipole moments  $\mu_i^{zx}$  ( $i = 1, 2, 3$ ) and a magnetic quadrupole moment  $Q_{zx}$ . In this figure, each  $\mu_i^{zx}$  is rotated by an angle  $\phi$  around the  $y$  axis with respect to that shown in Fig. 17(d). When  $\phi$  is small, the magnetic quadrupole moment  $Q_{zx}$  rotates at an angle  $\phi$  around the  $y$  axis without changing the direction of  $S_r$ . This implies that the degrees of freedom of the quadrupole moment are independent of degrees of freedom of the magnetic dipole moment. The coexistence of different kinds of independent degrees of freedom may lead to the generation of complex magnetic phase diagrams with subphases and unusual low energy collective excitations in  $\text{Gd}_3\text{Ru}_4\text{Al}_{12}$ . From this point of view, distorted, or breathing kagome lattices may be interesting subjects with which to study quadrupole orderings and novel low-energy collective excitations.

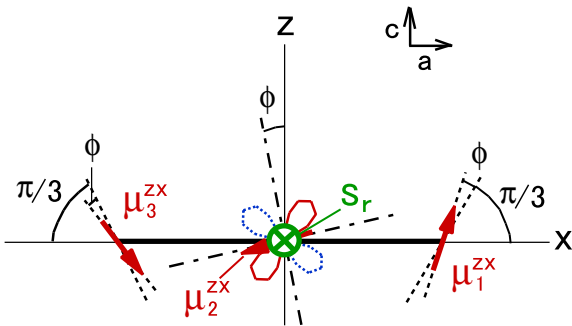


FIG. 21. Rotation of the magnetic quadrupole moment on a trimer. Each  $\mu_i^{zx}$  is rotated at an angle  $\phi$  around the  $y$  axis ( $b^*$  axis) with respect to that in Fig. 17(d). The green  $\otimes$  is  $S_r$  directed along the  $y$  axis.

## V. SUMMARY

We studied the spin system  $\text{Gd}_3\text{Ru}_4\text{Al}_{12}$ , which has inversion symmetry using macroscopic measurements. The FM trimer  $S_r$  is stable even in ordered phases, and  $\text{Gd}_3\text{Ru}_4\text{Al}_{12}$  is found to be the AFMTL that has certain degrees of strong anisotropies. The anisotropies appear to be generated in association with the formation of the FM trimer. The anisotropy becomes remarkably strong in the ordered states, and enabled the anisotropic magnetic phase diagrams to be determined. We found two types of anisotropic magnetic fields: a strong anisotropic field of the easy-plane type and a weak anisotropic field of the easy-axis type. The magnitude of the anisotropic energy of the former is approximately 12 K, and that of the latter is approximately 5 K. We additionally discussed the origin of the anisotropic fields. When the directivity of the component spins of an FM trimer is imperfect, the trimer carries magnetic quadrupole moments. We propose that the magnetic quadrupole interactions are the origin of the unusual magnetic anisotropies of  $\text{Gd}_3\text{Ru}_4\text{Al}_{12}$ . The quadrupole interaction among the linear combination of  $Q_p$  ( $p = yz, zx$ ) leads to an easy-plane-type anisotropic field, and that among  $Q_2^0$ s leads to an easy-axis-type anisotropic field. The initial fundamental unit, namely the  $\text{Gd}^{3+}$  ion, is not expected to be the origin of the magnetic anisotropy, but the FM trimer with imperfect directivity of the component spins becomes the origin of the anisotropy reflecting the structure of the distorted kagome lattice. The quadrupole interactions may supply the place of the DM interaction, and stabilize the helical structure at low fields. The imperfect directivity of component spins in FM trimers causes the degrees of the magnetic dipole freedom and the degrees of freedom of the magnetic quadrupole freedom to become independent under certain conditions. This may lead to additional subphase transitions and low-energy collective excitations in  $\text{Gd}_3\text{Ru}_4\text{Al}_{12}$ .

## ACKNOWLEDGMENT

The authors thank members of our laboratories S. Tanno, K. Hosokura, A. Ogata, M. Kikuchi, H. Moriyama, and N. Fukiage, Tohoku University, for the technical support they provided during our low-temperature experiments.

## APPENDIX A

As shown in Figs. 17 and 18, directions of  $S_r$ s are fixed to magnetic quadrupole moments  $Q$ s whose anisotropies reflect the structure of Gd triangle. It is expected that interactions among  $Q$ s work on  $S_r$ s as effective anisotropic fields. In the case of a hexagonal lattice, symmetric magnetic quadrupole moments are defined by the formula

$$Q_2^0 = \frac{1}{3} \int \rho_m(\mathbf{r}) (2z^2 - x^2 - y^2) d\mathbf{r}, \quad (\text{A1})$$

$$Q_2^2 = \frac{1}{2} \int \rho_m(\mathbf{r}) (x^2 - y^2) d\mathbf{r}, \quad (\text{A2})$$

$$Q_{xy} = \int \rho_m(\mathbf{r}) (xy) d\mathbf{r}, \quad (\text{A3})$$



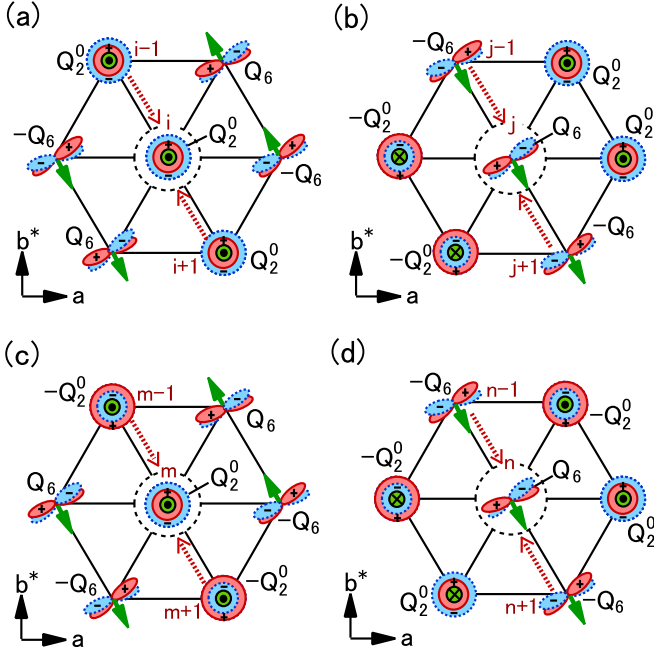


FIG. 22. [(a), (b)] An expected example of arrangement of magnetic quadrupole moments. [(c), (d)] Another example of arrangement of magnetic quadrupole moments. In this figure,  $Q_6$  denotes a linear combination of  $Q_{zx}$  and  $Q_{yz}$ . The dotted-red arrows indicate quadrupole interactions act on  $i, j, m, n$  sites from the nearest neighbors on the same Gd–Al plane, which does not cancel out. The other quadrupole interactions from the nearest neighbors on the plane cancel with each other out. The solid green arrows,  $\odot$  and  $\otimes$  filled with green color denote  $S_r$ .

and

$$Q_p = \int \rho_m(\mathbf{r}) p(x, y, z) d\mathbf{r}, \quad p(x, y, z) = yz, \quad zx, \quad (A4)$$

where  $\rho_m(\mathbf{r})$  is the density of magnetic charge. We summarized the magnitude of the magnetic quadrupole moments carried by the trimers depicted in Figs. 17 and 18 in Table I. The magnetic quadrupole interaction is expressed as

$$\begin{aligned} H_{QQ} = & - \sum_{i \neq j} G_1^{ij} \hat{Q}_2^0(i) \hat{Q}_2^0(j) \\ & - \sum_{i \neq j} G_5^{ij} [\hat{Q}_2^2(i) \hat{Q}_2^2(j) + \hat{Q}_{xy}(i) \hat{Q}_{xy}(j)] \\ & - \sum_{i \neq j} G_6^{ij} [\hat{Q}_{yz}(i) \hat{Q}_{yz}(j) + \hat{Q}_{zx}(i) \hat{Q}_{zx}(j)]. \end{aligned} \quad (A5)$$

Here,  $i$  and  $j$  are the indices of the trimer sites, and  $G_{ij}$  are the coupling constants.

## APPENDIX B

We assume arrangements of magnetic quadrupole moments shown in Fig. 22. The magnetic quadrupole interactions described in Eq. (A5) induce effective magnetic quadrupole fields (or quadrupole distributions of magnetic potential) in the neighborhood. Figure 22 describes examples of expected arrangements of magnetic quadrupole

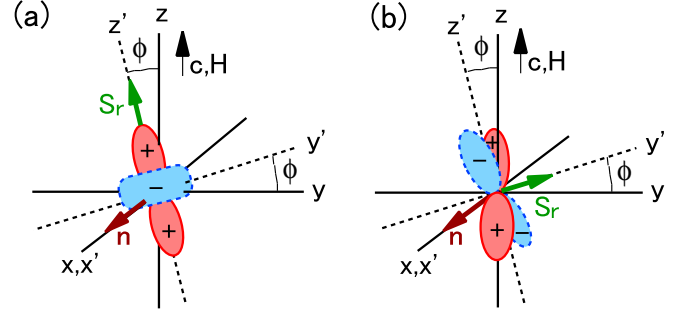


FIG. 23. (a) Magnetic charge distribution of  $\rho(r') \frac{1}{3}(2z'^2 - x'^2 - y'^2)$ , where  $\rho(r')$  is the function that only depends on the radius  $r'$ . Here,  $\rho(r')$  is normalized as described in the text. The unit vector  $\mathbf{n} = (1, 0, 0)$  in the  $x - y - z$  coordinate denotes the axis of rotation. The relation between the coordinates  $x' - y' - z'$  and  $x - y - z$  is defined by Eqs. (B7) and (B8). The angle  $\phi$  is the angle between  $z$  axis and  $z'$  axis. (b) Magnetic charge distribution of  $\rho(r')(z'x')$ , where  $\rho(r')$  is the function that only depends on the radius  $r'$ . The unit vector  $\mathbf{n} = (1, 0, 0)$  in the  $x - y - z$  coordinate denotes the axis of rotation. The relation between the coordinate  $x' - y' - z'$  and  $x - y - z$  is defined by Eqs. (B7) and (B8). The angle  $\phi$  is the angle between the  $y$  axis and  $y'$  axis. Here, the  $y$  axis is in the opposite direction of the  $b$  axis.

moments. A set of Figs. 22(a) and 22(b) is an example and that of Figs. 22(c) and 22(d) is another example. Here, we only consider the quadrupole interactions between the nearest neighbors in the same Gd–Al plane. The dotted red arrows in Fig. 22 denote the quadrupole interactions, which do not cancel with each other out. In Fig. 22(a), the interactions from  $Q_6$ -type moments to the  $Q_2^0$  on  $i$  site cancel with each other out. Under weak applied fields along the  $c$  axis, these  $Q_6$ -type moments are tilted by the applied fields but this cancellation is not affected. On the other hand, quadrupole interactions between  $(i, i - 1)$  sites and that between  $(i, i + 1)$  sites reinforce each other. The magnetic quadrupole fields at  $i$  site is, therefore, expressed as

$$Q^{af}(i) = 2G_1 Q_2^0, \quad (B1)$$

at zero field. For the same reason, quadrupole fields at  $j, k, m, n$  sites are expressed as

$$Q^{af}(j) = -2G_6 Q_6, \quad (B2)$$

$$Q^{af}(m) = -2G_1 Q_2^0, \quad (B3)$$

$$Q^{af}(n) = -2G_6 Q_6, \quad (B4)$$

respectively. As shown in Fig. 22, the trimers are separated into two groups. One carries  $Q_2^0$  moments and is under  $Q_2^0$ -type quadrupole fields, the other carries  $Q_6$  moments and is under  $Q_6$ -type quadrupole fields. Quadrupole interactions between these subsystems of trimers are canceled with each other out.

Here, we discuss the anisotropies induced by the quadrupole interactions. We calculate changes in energy when magnetic quadrupole moments are rotated artificially under quadrupole fields to examine the anisotropies. In Fig. 23(a), the magnetic charge distribution of  $\rho_m(r')$  of  $Q_2^0$  type is illustrated. In this figure  $z$  axis is parallel to the  $c$  axis. The

distribution of magnetic charge is expressed as

$$\rho(r') \frac{1}{3}(2z'^2 - x'^2 - y'^2) \quad (\text{B5})$$

using the  $x' - y' - z'$  coordinate, where  $\rho(r')$  is the function that depends only on the radius  $r'$ . The function  $\rho(r')$  is normalized as

$$Q_2^0 = \frac{1}{3} \int \rho(r') (2z'^2 - x'^2 - y'^2) dx' dy' dz'. \quad (\text{B6})$$

The direction of  $S_r$  is parallel to the  $z'$  axis as illustrated in Figs. 18(e) and 18(f). As shown in Fig. 23(a), we define rotation around the unit vector  $\mathbf{n} = (1, 0, 0)$  with a small angle  $\phi$  as

$$R_1 = \begin{pmatrix} 1 & 0 & 0 \\ 0 & \cos \phi & -\sin \phi \\ 0 & \sin \phi & \cos \phi \end{pmatrix}. \quad (\text{B7})$$

The relation between the two coordinates in Fig. 23(a) is given as

$$(x', y', z') = R_1(x, y, z). \quad (\text{B8})$$

and the magnetic distribution expressed in the  $x - y - z$  coordinate is

$$\begin{aligned} \rho_m(\mathbf{r}) &= R_1 \left[ \rho(r) \frac{1}{3}(2z^2 - x^2 - y^2) \right] \\ &= \rho(r) \left[ \left(-\frac{1}{2} + \frac{3}{2} \cos^2 \phi\right) \frac{1}{3}(2z^2 - x^2 - y^2) \right. \\ &\quad \left. - \sin^2 \phi \frac{1}{2}(x^2 - y^2) + 2 \cos \phi \sin \phi (yz) \right]. \end{aligned} \quad (\text{B9})$$

Therefore, quadrupole moment on  $i$  site in Fig. 23(a) is described as a function of  $\phi$  in the  $x - y - z$  coordinate as

$$\begin{aligned} Q_2^0(\phi) &= Q_2^0 \left(-\frac{1}{6} + \frac{1}{2} \cos^2 \phi\right) \\ &\quad - \sin^2 \phi Q_2^0 + 2 \cos \phi \sin \phi Q_{yz}. \end{aligned} \quad (\text{B10})$$

As described in Eq. (B1), this  $Q_2^0(\phi)$  is under the quadrupole field  $Q^{qf}(i)$ . The change in the energy concerning the quadrupole interactions is described as

$$E_a^i(\phi) = -G_1(Q_2^0)^2 \cos^2 \phi \quad (\text{B11})$$

except for constant difference. When the sign of  $G_1$  is positive, this indicates an effective easy-axis-type anisotropy.

Next, we discuss the anisotropy on  $j$  site in Fig. 22(b). Figure 23(b) shows the illustration of the charge distribution of  $\rho_m(\mathbf{r}')$  of  $Q_{zx}$  type. The magnetic charge distribution is given by

$$\rho_m(\mathbf{r}') = \rho(r')(z'x') \quad (\text{B12})$$

in the  $x' - y' - z'$  coordinate. The function  $\rho(r')$  is normalized as

$$Q_{zx} = \int \rho(r')(z'x') dx' dy' dz'. \quad (\text{B13})$$

The direction of  $S_r$  is in the  $y'$  axis as we can see from Fig. 17. In Fig. 23(b), the rotation around the unit vector  $\mathbf{n} = (1, 0, 0)$  denotes the axis of rotation. The angle  $\phi$  is defined as the angle between  $y$  and  $y'$  axes, and the rotation is expressed as Eq. (B7). This rotation can be induced by a weak applied field directed along the  $z$  axis (along the  $c$  axis). The magnetic charge distribution in  $x - y - z$  coordinate is expressed as

$$\rho_m(\mathbf{r}) = \rho(r)(\sin \phi xy + \cos \phi zx) \quad (\text{B14})$$

in the  $x - y - z$  coordinate. Therefore, the magnetic quadrupole moment on  $j$  site in Fig. 22(b) is described as

$$Q_{zx}(\phi) = \sin \phi Q_{xy} + \cos \phi Q_{zx} \quad (\text{B15})$$

in this coordinate. As shown in Fig. 22(b), this moment is under the quadrupole fields made by the quadrupole moments on  $j - 1$  and  $j + 1$  sites. These moments on  $j - 1$  and  $j + 1$  sites are also tilted by the applied field with the angle  $\phi$ . Therefore, the quadrupole field induced on  $j$  site is given by

$$Q^{qf}(j) = 2[G_5 \sin \phi (-Q_{xy}) + G_6 \cos \phi (-Q_{zx})]. \quad (\text{B16})$$

The change in the energy concerning the quadrupole interactions is described as

$$E_a^j(\phi) = -2[G_6(Q_{zx})^2 - G_5(Q_{xy})^2] \sin^2 \phi \quad (\text{B17})$$

except for constant difference. When the sign of  $[G_6(Q_{zx})^2 - G_5(Q_{xy})^2]$  is negative, this gives an effective easy-plane-type anisotropy in the range of weak applied field.

If we assume some special magnetic quadrupole arrangements, trimers are separated to two sub-systems. Because the magnetic quadrupole interactions between these sub-systems are weak, different magnetic anisotropies can coexist in  $\text{Gd}_3\text{Ru}_4\text{Al}_{12}$ .

[1] J. Niermann and W. Jeitschko, *Z. Anorg. Allg. Chem.* **628**, 2549 (2002).  
 [2] K. Momma and F. Izumi, *J. Appl. Crystallogr.* **44**, 1272 (2011).  
 [3] W. Ge, H. Ohta, C. Michioka, and K. Yoshimura, *J. Phys.: Conf. Ser.* **344**, 012023 (2012).  
 [4] W. Ge, C. Michioka, H. Ohta, and K. Yoshimura, *Solid State Commun.* **195**, 1 (2014).  
 [5] R. Troć, M. Pasturel, O. Tougaard, A. P. Sazonov, A. Gukasov, C. Sułkowski, and H. Noël, *Phys. Rev. B* **85**, 064412 (2012).  
 [6] D. I. Gorbunov, M. S. Henriques, A. V. Andreev, V. Eigner, A. Gukasov, X. Fabrèges, Y. Skourski, V. Petříček, and J. Wosnitza, *Phys. Rev. B* **93**, 024407 (2016).

[7] S. Nakamura, S. Toyoshima, N. Kabeya, K. Katoh, T. Nojima, and A. Ochiai, *JPS Conf. Proc.* **3**, 014004 (2014).  
 [8] S. Nakamura, S. Toyoshima, N. Kabeya, K. Katoh, T. Nojima, and A. Ochiai, *Phys. Rev. B* **91**, 214426 (2015).  
 [9] D. I. Gorbunov, M. S. Henriques, A. V. Andreev, A. Gukasov, V. Petříček, N. V. Baranov, Y. Skourski, V. Eigner, M. Paukov, J. Prokleška, and A. P. Gonçalves, *Phys. Rev. B* **90**, 094405 (2014).  
 [10] V. Chandragiri, K. K. Iyer, and E. V. Sampathkumaran, *Intermetallics* **76**, 26 (2016).  
 [11] V. Chandragiri, K. K. Iyer, and E. V. Sampathkumaran, *J. Phys.: Condens. Matter* **28**, 286002 (2016).  
 [12] R. B. Griffiths, *Phys. Rev. Lett.* **23**, 17 (1969).

- [13] S. Nakamura, N. Kabeya, M. Kobayashi, K. Araki, K. Katoh, and A. Ochiai, *Phys. Rev. B* **98**, 054410 (2018).
- [14] T. Matsumura, Y. Ozono, S. Nakamura, and N. Kabeya, and A. Ochiai, *J. Phys. Soc. Jpn.* **88**, 023704 (2019).
- [15] M. Hirschberger, T. Nakajima, S. Gao, L. Peng, A. Kikkawa, T. Kurumaji, M. Kriener, Y. Yamasaki, H. Sagayama, H. Nakao *et al.*, *Nat. Commun.* **10**, 5831 (2019).
- [16] S. D. Yi, S. Onoda, N. Nagaosa, J. H. Han, *Phys. Rev. B* **80**, 054416 (2009).
- [17] S. Buhrandt and L. Fritz, *Phys. Rev. B* **88**, 195137 (2013).
- [18] R. Kubo, *Phys. Rev.* **87**, 568 (1952).
- [19] C. Kittel, in *Quantum Theory of Solids*, (John Wiley and Sons Inc., New York, 1964) p. 62.
- [20] V. Jaccarino, in *Magnetism*, edited by G. T. Rado and H. Suhl (Academic Press, New York, 1965), Vol. IIA, p. 319.